



ELSEVIER

Physica D 144 (2000) 434–445

PHYSICA D

www.elsevier.com/locate/physd

# Influence of phase transition on pattern formation during catalytic reactions

R.F.S. Andrade\*, D. Lima, F.B. Cunha

*Instituto de Física, Universidade Federal da Bahia, Campus da Federação, 40210-340 Salvador, Ba., Brazil*

Received 1 November 1999; received in revised form 28 February 2000; accepted 27 March 2000

Communicated by A. Doelman

## Abstract

We investigate the influence of the order of surface phase transitions on pattern formation during chemical reaction on mono-crystal catalysts. We use a model consisting of two partial differential equations, one of which describes the dynamics of the surface state with the help of a Ginzburg–Landau potential. Second- or first-order transitions are described by decreasing or increasing the relative value of the third-order coefficient of the potential. We concentrate on the stability of spiral patterns, and determine the region of the diagram where plane waves, asymptotic solutions of the spiral arms far from the core, are Benjamin–Feir unstable. The results indicate that spiral patterns are much more abundant when the transition is of second order, which is corroborated by the numerical integration of the equations of motion. Results also find support on the experiments, which show a rich pattern selection for the CO oxidation on Pt(1 1 0), but fail to detect the same behavior when the surface is Pt(1 0 0). © 2000 Elsevier Science B.V. All rights reserved.

PACS: 05.45.-a; 47.54.+r; 68.35.Rh; 82.20.Mj

Keywords: Phase transition; Pattern formation; Catalytic reaction; Ginzburg–Landau potential

## 1. Introduction

Pattern formation during low pressure isothermal chemical reactions on mono-crystal catalysts strongly depends on the interplay among chemical kinetics and crystalline arrangement of the surface. Such effects are well documented through several experiments with different reactants and mono-crystal surfaces [1–3]. The general mechanism leading to oscillatory behavior is based on the existence of two different surface states, where only one of them has catalytic activity. The details of chemical kinetics and surface phase transformations control the spatio-temporal structures which the system may develop.

One of the most simple situations consists of the CO oxidation on a platinum surface [4]. Oscillatory behavior has been reported when the exposed surface has (1 1 0) and (1 0 0) crystallographic orientations [5–11]. The two systems share many similar features: they follow simple Langmuir–Hinshelwood kinetics; they exhibit phase transitions

\* Corresponding author. Tel.: +55-71-247-2033; fax: +55-71-235-5592.  
E-mail address: randrade@ufba.br (R.F.S. Andrade).

between a low energy arrangement for the clean surface, and the reconstructed state, which follows the bulk orientation and is stabilized by the presence of reactants; they are catalytically active only when the surface is in the reconstructed state.

Despite the overall similar characteristics sketched above, it is observed that the (1 1 0) surface has a much richer set of spatio-temporal patterns [12]. Several types of patterns (plane waves, spirals, standing waves, and so on) have been reported in many experiments [13–16] and also in the analysis of the partial differential equations modeling the system [17–19]. On the other hand, the (1 0 0) counterpart displays only the traveling waves pattern. Even though it is not sufficiently clear whether they can exist in a true homogeneous surface, or whether they are produced by surface inhomogeneities [6,20,21].

Such different behavior must be traced back to the details of the dynamics of the two systems, which can be cast into two groups: those related to the chemical kinetics and those originating from the mechanisms of phase transitions. Two main differences observed in the chemical kinetics are: (i) the presence of the trapping and untrapping from adsorbed CO from the *hex* to the  $1 \times 1$  phase in the (1 0 0) system; and (ii) the clear precursor adsorption dynamics for the (1 1 0) system, while the adsorption of CO on Pt(1 0 0) is inhibited linearly by preadsorbed CO. However, the major difference between the two systems is the nature of the phase transition. The (1 1 0) surface undergoes a second-order phase transition from the  $(1 \times 1)$  to the  $(1 \times 2)$  state, in contrast to the first-order transition from the  $(1 \times 1)$  to the *hex* state of the (1 0 0) surface.

We think it is important to identify which steps are actually essential for the rich patterns shown by the (1 1 0) system. The purpose of this work is to address this question. However, instead of looking for all possible factors, we focus on the effect of the nature of the phase transitions only. As the models for Pt(1 0 0) and Pt(1 1 0) incorporate slight differences in the chemical steps, our task can be better pursued if we work with one single model, hold constant all terms describing the chemical dynamics, and induce changes in the nature of the phase transitions.

We consider the model introduced some years ago [21–23] (ADB) to describe the oscillations in the (1 0 0) system consisting of a set of four coupled partial differential equations (PDE). The advantage of this model for the purpose sketched before is the description of the phase transitions by a Ginzburg–Landau potential (GLP). The original version of this potential includes a cubic term, which is necessary to describe the first-order transition [24]. If we decrease the magnitude of the cubic coefficient, the energy barrier between the *hex* and the  $(1 \times 1)$  phases is reduced. Hence, we easily obtain a situation where the surface phase transition is similar to that observed in Pt(1 1 0).

In our investigation, we have taken two sets of parameters, each one describing the first- and second-order situations, and analyzed the emergence and stability of spiral patterns, while all other parameters associated to the chemical kinetics were kept constant. Since the stability diagram for the fixed points (FP) of the model has been well characterized, we have concentrated our investigation on the region of partial pressures where no steady state (stable FP) is available. Our results were obtained by two different methods: the numerical integration of the PDE and a stability analysis of the amplitude equations for the plane waves which emerge as the subcritical Hopf bifurcation line is crossed. The analysis of the perturbations in the long wavelength limit sets the border of the Benjamin–Feir stability region [25], that is an upper bound for the stability of spiral patterns. The results from both methods indicate that the emergence of spiral patterns is more likely for the GLP which mimics the second-order transition.

The rest of this article is organized as follows. In Section 2, we discuss the main features of the model indicating how the situations corresponding to first and second-order transitions will be described. In Section 3, the stability analysis for plane waves is presented and the Benjamin–Feir unstable region is drawn for both diagrams. Results obtained by the numerical integrations of the system are presented in Section 4. Section 5 closes the article with our concluding remarks.

## 2. The model

Experimental observations indicate that the free  $1 \times 1$  Pt(1 0 0) surface is not stable [5,7], so that it spontaneously reconstructs into a quasi-hexagonal hex phase. CO adsorb on both surface states, but  $O_2$  adsorbs dissociatively only on the  $1 \times 1$  phase. If CO and  $O_2$  adsorb and react on the  $1 \times 1$  catalytic active phase, after a burst of intense  $CO_2$  production,  $1 \times 1$  patches empty out, driving the surface to the (catalytic inert) hex phase. This situation is reversed when CO molecules adsorb on this phase inducing a hex  $\rightarrow 1 \times 1$  transition.

The back and forth switch between the two surface arrangements is the actual mechanism for the complex behavior of the system [7]. While most experimental details of this system have been known for over 15 years [5–8], only recent experimental results have cleared out that a small cluster of 4–5 CO molecules are necessary to nucleate a small  $1 \times 1$  island within the hex substrate [9–11] indicating a nonlinear dependence on the local CO coverage.

The ADB model was introduced about 10 years ago. It takes into account most of the experimental facts indicated above, while its major innovation is the utilization of a microscopic surface site interaction model to describe the phase transition dynamics. Herein, the surface is described by a set of discrete site variables. They assume discrete values, that are associated to the possible states in which the surface may exist. A Hamiltonian accounts for the interaction energy that depends on the states of each microscopic variable, while the methods of statistical mechanics are used to obtain the free energy and other thermodynamical properties of the surface. This procedure, first extensively used for the analysis of *equilibrium* states of a surface [26], has also been recently employed for the description of *non-equilibrium* situations [27]. We remark that the time-scale of the local processes on the surface, associated to the states of the microscopic site variables is much shorter than the time-scale in which macroscopic oscillations are observed. So the hypothesis of local equilibrium justifies the use of the methods of equilibrium statistical mechanics to a dynamical situation.

The ADB model is written in terms of four space and time dependent variables, namely  $u_a$ ,  $u_b$ ,  $v_a$  and  $a$  [21,22]. They describe, respectively, the fractions of  $1 \times 1$  and hex sites occupied by adsorbed CO, of  $1 \times 1$  sites occupied by O atoms, and of surface sites in the  $1 \times 1$  phase. The equations read as follows:

$$\frac{\partial u_a}{\partial t} = ak_1 P_{CO} - k_2 u_a + k_3 a u_b - k_4 \frac{u_a v_a}{a} + k_5 \nabla^2 u_a, \quad (2.1)$$

$$\frac{\partial u_b}{\partial t} = (1 - a)k_1 P_{CO} - k_6 u_b - k_3 a u_b, \quad (2.2)$$

$$\frac{\partial v_a}{\partial t} = ak_7 P_{O_2} \left[ \left( 1 - \frac{sv_a}{a} - \frac{ru_a}{a} \right)^2 + \alpha \left( 1 - \frac{sv_a}{a} \right)^2 \right] - k_4 \frac{u_a v_a}{a}, \quad (2.3)$$

$$\frac{\partial a}{\partial t} = k_8 \left[ \frac{u_a + v_a}{a} - \bar{\eta}_2 a - \bar{\eta}_3 a^2 - \bar{\eta}_4 a^3 \right] + k_9 \nabla^2 a. \quad (2.4)$$

$P_{CO}$  and  $P_{O_2}$  indicate the partial pressures of the two reactants.  $k_1$ ,  $k_2$ ,  $k_6$  and  $k_7$  denote the coefficients for adsorption and desorption, while  $r$  and  $s$  account for the inhibition caused in the  $O_2$  adsorption by preadsorbed CO and O. Further decrease on  $O_2$  adsorption is induced by surface defects described by the parameter  $\alpha$ .  $k_4$  controls the reaction step, while  $k_3$  is related to the trapping mechanism for CO consisting of microscopic migration from an hex site to a neighboring empty  $1 \times 1$  site. It should be mentioned that the recent indication of the reverse untrapping mechanism will not change the nature of our results, mainly because the untrapping constant is much smaller than  $k_3$  [28,29]. Normal physical diffusion of CO on  $1 \times 1$  patches is described by  $k_5$ . The constant  $k_8$  gauges the time-scale of the phase transition dynamics, while  $k_9$  describes the stress resulting from a variation of the state of the surface with space, similar to the phenomenon observed for domain walls in magnetism [30]. Values for all parameters of the model used herein are listed in Table 1.

Table 1  
Values for the coefficients used in the system (1)–(2)<sup>a</sup>

		Value in this work
<i>Constants</i>	$k_1$	$2.5 \times 10^5 \text{ ML s}^{-1} \text{ Torr}^{-1}$
	$k_2$	$1 \text{ s}^{-1}$
	$k_3$	$50 \text{ s}^{-1}$
	$k_4$	$10^2\text{--}10^5 \text{ ML Torr}^{-1}$
	$k_5$	$10^{-4}\text{--}10^{-3} \text{ cm}^2 \text{ s}^{-1}$
	$k_6$	$10 \text{ s}^{-1}$
	$k_7$	$5.6 \times 10^4 \text{ ML s}^{-1} \text{ Torr}^{-1}$
	$k_8$	$1 \text{ s}^{-1}$
	$k_9$	$10^{-4}\text{--}10^{-1} \text{ cm}^2 \text{ s}^{-1}$
	$r$	2
<i>First set of GL coefficients</i>	$s$	$\frac{5}{3}$
	$\bar{\eta}_2$	4
	$\bar{\eta}_3$	–10
	$\bar{\eta}_4$	7
<i>Second set of GL coefficients</i>	$\bar{\eta}_2$	4
	$\bar{\eta}_3$	–9.2
	$\bar{\eta}_4$	6.4

<sup>a</sup>They are essentially the same used in [21]. The last entries correspond to the new values of the GLP coefficients used to model the second-order phase transition.

Eq. (2.4), that describes the surface phase transition between the  $1 \times 1$  and hex states, results from the minimization of the GLP

$$g_{\text{GL}}(a) = \int_S \rho [-\epsilon_1 \theta_a a - \eta_2 a^2 - \eta_3 a^3 - \eta_4 a^4 + \frac{1}{2} k_9' (\nabla a)^2] dS. \quad (2.5)$$

(2.5) is an approximation to the mean-field free energy of the site interaction model, where the coefficients  $\eta_n = \bar{\eta}_n/n$  result from the expansion of the free energy in powers of  $a$ . A full discussion of the site model and the derivation of the GLP can be found in [21,22]. It is also shown that both the free energy and GLP describe key steps of the adsorption and phase transition phenomena. The use of (2.5) simplifies the stability analysis of the FPs of the model and the bifurcation diagram. Indeed, it leads to a polynomial form for the evolution equation (2.4), which contrasts to a complex expression containing logarithms resulting from the minimization of the free energy. The other symbols in (2.5) are related to the microscopic site model, but their influence is embedded in the constants  $k_8$  and  $k_9$ .

The description of phase transition based on this procedure contrasts to the phenomenological approach in which experimental observations are translated into rate equations in a step wise way (usually two or three expressions are required for the description of the rate of change of the surface [6,19,28,29]). However, independent of the different assumptions used for the derivation of the equations of motion, the corresponding nullclines of the distinct models share the same sigmoidal shape. This explains why the phase space for different models have a similar structure.

The ADB model (2.1)–(2.4) is able to quantitatively reproduce the experimental facts (temperature hysteresis loop at constant CO pressure, oscillating regions in the phase diagram, emergence of traveling waves, etc.) with a good degree of accuracy. This indicates that despite some simplifications in the kinetics, it captures the essential steps of the process.

For the actual values of the constants of the ADB model, the linear stability analysis for all of its FPs indicates a fast relaxing dynamics for two directions in phase space (eigenvalues of the linear stability matrix are  $\lambda_1 \sim k_4 \sim 10^5$  and  $\lambda_2 \sim k_3 \sim 10^2$ ). An adiabatic elimination of these fast relaxing modes reduces the original model to the

following reduced system of two PDEs [21], on which we actually base our investigation:

$$\frac{\partial w}{\partial t} = ak_1 P_{CO} \frac{1+q}{1+aq} - k_2 \frac{(w+|w|)}{2} + \Theta(\omega)k_5 \nabla^2 w - ak_7 P_{O_2} \left[ \left( 1 - \frac{(r-s)w + (r+s)|w|}{2a} \right)^2 + \alpha \left( 1 - \frac{s(w-|w|)}{2a} \right)^2 \right], \quad (2.6)$$

$$\frac{\partial a}{\partial t} = k_8 \left[ \frac{|w|}{a} - \bar{\eta}_2 a - \bar{\eta}_3 a^2 - \bar{\eta}_4 a^3 \right] + k_9 \nabla^2 a. \quad (2.7)$$

$\Theta(\omega)$  indicates the Heaviside function,  $q = k_3/k_6$ , and the new variable  $w$  is defined as

$$w = u_a - v_a + \frac{aqu_b}{1+aq}. \quad (2.8)$$

The results produced by (2.1)–(2.4), and (2.6) and (2.7) systems are quite similar, especially in the  $k_4 \rightarrow \infty$  limit. Working with the reduced ADB model (2.6) and (2.7) has many advantages: the effort required for the analytical expansions, evaluation of FPs and linear stability are considerably reduced; for numerical computations, the use of memory is cut by the half, as only two variables are now used; the CPU time is reduced by a much large factor, mainly because the restriction of very small integration steps, imposed by the large value of  $k_4$  can be released.

The GLP description introduced by the ADB model offers an adequate framework for the present investigation. Starting from the original values for the  $\eta_n$ , which are tuned to describe a very specific experimental system with first-order transition, we can choose other values for these coefficients in order to mimic a situation of a second-order transition. For this purpose it is necessary to reduce the value of  $\eta_3$  with respect to  $\eta_2$  and  $\eta_4$ , making the potential barrier between the two different surface states very small as illustrated in Fig. 1. The values for the two sets of  $\eta_n$  used in Fig. 1 are also listed in Table 1. Henceforth, we refer to sets 1 (original ADB) and 2 to describe, respectively, the situations of first- and second-order transitions used in our investigation.

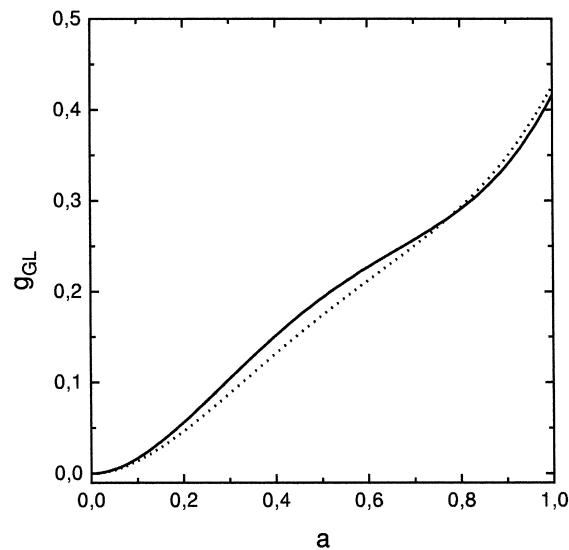


Fig. 1. Plot of the two GLPs used in this work (when  $\theta_a = 0$ ). The solid and dashed curves correspond to the first and second set of coefficients listed in Table 1. When the relative value of  $\eta_3$  decreases, the form of the potential mimics a second-order transition.

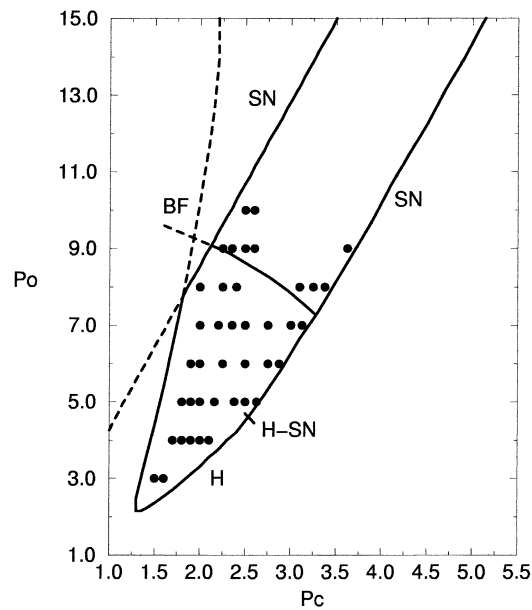


Fig. 2. Phase diagram in the  $P_C \times P_O$  plane ( $P_C = 2rk_1 P_{CO}$ ,  $P_O = 2rk_4 P_{O_2}$ ) for the first set of parameters in Table 1. The solid SN and H/SN (respectively, saddle-node and Hopf bifurcation) lines form the border to the region with no stable FP for the homogeneous system. They continue to exist in the region with at least one stable FP, and are indicated with dashes. The BF line indicates the limit of Benjamin–Feir stability (3.4), and spirals are expected within the region bounded by H, H/SN and BF. The solid points indicate the loci where numerically stable spirals were observed.

The ADB model (either in the original or reduced version) has a large number of FPs, some of which coexist for some intervals of partial pressures. The linear stability for all FPs in (2.6) and (2.7) indicates multi-stability of steady states and coexistence of oscillatory behavior and time independent solutions, what is corroborated by the numerical integration of the model [21]. For the sake of simplicity, the phase diagrams, for the two set of parameters of the GLP shown in Figs. 2 and 3, locate only the minimal oscillatory region, i.e., where no stable FP exists. Figs. 2 and 3 contain further information about the stability of spiral waves that will be discussed in the next sections. There, we concentrate our analysis on the minimal oscillatory region, in order to avoid the presence of competition among steady states and oscillatory solutions.

The model is sensible to the values of the GLP coefficients. For the set 2, the region of unstable FPs became thinner and moved to larger values of  $P_{CO}$  and  $P_{O_2}$ . The actual instability region for Pt(1 1 0) is also much smaller than that of the Pt(1 0 0) surface [19], so that the changes, we obtained for the new set of GLP coefficients are in accordance with the experiments.

### 3. Stability of amplitude solutions

The phase diagram comprises several Hopf or saddle-node bifurcation lines, corresponding to the change of stability or to the collapsing of pairs of FPs. The border to the minimal oscillatory region is formed by pieces of several such lines as shown in Figs. 2 and 3. Close to the Hopf bifurcation line, it is possible to use the Benjamin–Feir (BF) stability criterion [31] to the analysis of the stability of spiral waves. The procedure is based on the behavior of the amplitude  $A(R, T)$  of the oscillatory solution, that is described by the following universal amplitude equation [31]:

$$\frac{\partial A}{\partial T} = A - (1 + i\beta)|A|^2 A + (1 + i\epsilon)\nabla^2 A. \quad (3.1)$$

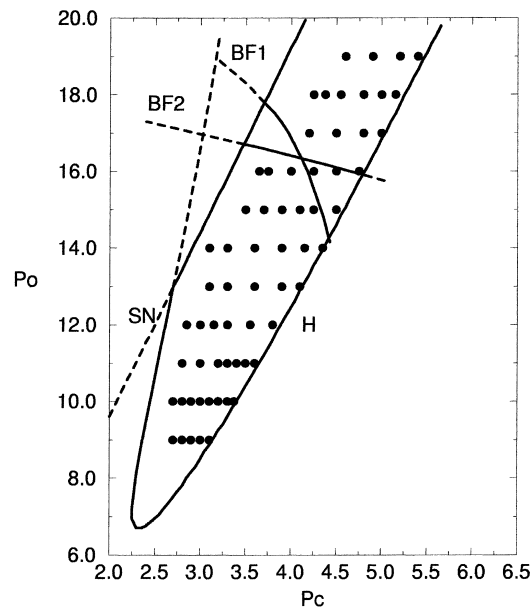


Fig. 3. Phase diagram in the  $P_C \times P_O$  plane for the second set of parameters in Table 1. The border to the region with no stable FP is formed by one SN and one H line. The BF1 and BF2 lines indicate the Benjamin–Feir stability limits evaluated for points in the left and right side of the H line. Spirals now are expected within the region bounded by H and SN, below the BF1 and above the BF2 line. As in Fig. 2, the solid points indicate numerically stable spirals.

The  $\beta$  and  $\epsilon$  coefficients, which depend both on the model and on the coordinates of the FP can be derived by several different approaches. We have used the operator technique introduced by Kuramoto and Tsuzuki [32]. The most important expressions used for the evaluation of  $\beta$  and  $\epsilon$  are presented in Appendix A. As the FPs of the model (2.6) and (2.7) can only be found by numerical means, it is not possible to express  $\beta$  and  $\epsilon$  in a closed analytical form.

Approximate results for the stability of spiral waves can be obtained with the help of (3.1). It is straightforward to see that it admits plane wave solutions of the form

$$A = A_0 \exp[i(\boldsymbol{\kappa} \cdot \mathbf{R} - \omega T)], \quad (3.2)$$

where  $A_0^2 = 1 - \kappa^2$  and  $\omega = \beta + (\epsilon - \beta)\kappa^2$ . Such solutions also describe the wave fronts formed by the spiral arms very far from the core region. Therefore, the stability of the plane waves represents an upper bound for the stability of the spirals. The stability analysis of the plane waves becomes even simpler if we restrict ourselves to longitudinal perturbations of the form

$$A' \sim \exp(\pm i\mathbf{q} \cdot \mathbf{R}), \quad \mathbf{q} \parallel \boldsymbol{\kappa}, \quad (3.3)$$

where  $\mathbf{q}$  is its wave vector. At the long wavelength limit ( $\mathbf{q} \rightarrow 0$ ), we obtain the criterion for the BF stability [32], which can be written in terms of the coefficients in (3.1) as

$$D_{\parallel} = 1 + \beta\epsilon > 0. \quad (3.4)$$

Further analysis of spiral stability taking into account the effect of the core and of finite wavelength perturbation have been developed recently [25,33]. They indicate only slight differences of the stability region in comparison to that obtained by the BF criterion. Hence, due to the complexity of the bifurcation diagram of our model, we have restricted ourselves to the simpler analysis expressed by (3.4). The regions for the BF stable spirals are also indicated

in Figs. 2 and 3. For the first set of coefficients, the BF region is obtained when we consider the Hopf bifurcation at the left-hand side of the FP unstable region, and it is bounded by the BF line to the lower part of the FP unstable region. We observe that BF stability is obtained even for values of  $P_{O_2}$ , where the left border of the diagram corresponds to a saddle-node bifurcation. This is possible because a Hopf line still exists close to that region. However, on increasing  $P_{O_2}$  the distance from the Hopf line to the FP unstable region increases and the BF stability is lost. For even larger values of  $P_{O_2}$  the Hopf line disappears. The rest of the border of the FP unstable region is formed by saddle-node bifurcation lines, and the stability analysis of the solutions of the amplitude equation (3.1) fails.

For set 2, the right border of the FP unstable region corresponds to a Hopf bifurcation. So it is possible to perform the BF stability analysis both on the right and left (for relative smaller values of  $P_{O_2}$ ) sides. We have found that the indications from the left Hopf line are qualitatively similar to that described before (line BF1 in Fig. 3). However, the right side line has a complementary effect: for small values of  $P_{O_2}$  it indicates BF instability, changing into stability as  $P_{O_2}$  increases (line BF2). This change occurs almost at the same point where the left side line stability is lost. So, for practical purposes, BF stability is observed for the whole FP unstable region.

The above analysis indicates that an enhancement of the first-order character of the surface phase transition decreases the likelihood of stable spiral patterns. From the physical point of view the increase of the barrier described by the coefficient  $\eta_3$  hardens the transition process and favors the existence of hysteresis loops. From the mathematical point of view this corresponds to a change from a Hopf to a saddle-node bifurcation line, which decreases the regions of BF stability. As we see in the next section, the numerical integration of the system (2.6) and (2.7) corroborates the results of the stability analysis.

#### 4. Numerical integration

We have performed several numerical integrations of the system (2.6) and (2.7) in square grids up to  $256 \times 256$  cells. Time evolution was computed by a fourth-order Runge–Kutta algorithm, while the Laplacian diffusion operator takes into account the two nearest neighbor cells in each direction. In order to investigate the development and stability of spiral patterns for the different values of  $P_{CO}$  and  $P_{O_2}$ , we settled initial conditions in three different ways: (i) create a single topological discontinuity in the center of the grid, choosing for each quadrant points of the stable limit cycle for the particular values of the partial pressures; (ii) generate patches ( $\sim 16 \times 16$  cells) with the same value, randomly taken from stable limit cycles at different instants of time; (iii) move from a neighboring place with a fully developed and stabilized spiral. The results summarized below take into account integrations performed with these different initial conditions. The regions of numerically stable spirals are also included in Figs. 2 and 3.

The results indicate a reasonable concordance with those obtained from the stability analysis of amplitude equations. Spirals are easily formed with any of the methods quoted above. For a fixed value of  $P_{O_2}$  the spiral wavelength increases when  $P_{CO}$  is decreased. For set 1, Fig. 2 shows that on increasing  $P_{O_2}$ , spirals become numerically unstable in the middle of the region, even below the BF line. On the other hand, they remain numerically stable close to the border after the BF line is crossed. For smaller  $P_{O_2}$ , we find a discrepancy in the region close to the left border formed by the Hopf line: spirals are numerically unstable exactly in the region where  $D_{||}$  has the largest values, i.e., in the region where they should be most stable. We conjecture that spirals are destabilized by other structures in the phase space, e.g., the saddle-node bifurcation (SN line in Fig. 2). For still smaller values of  $P_{O_2}$  the region becomes bounded by a single Hopf line, and the loss of stability of spirals close to the border may depend on the interplay of competing Hopf cycles.

For set 2, the region for numerically stable spirals is also larger, which confirms the general tendency of the results presented in Section 3. As for set 1, the spiral wavelength increases when  $P_{CO}$  decreases. The presence of

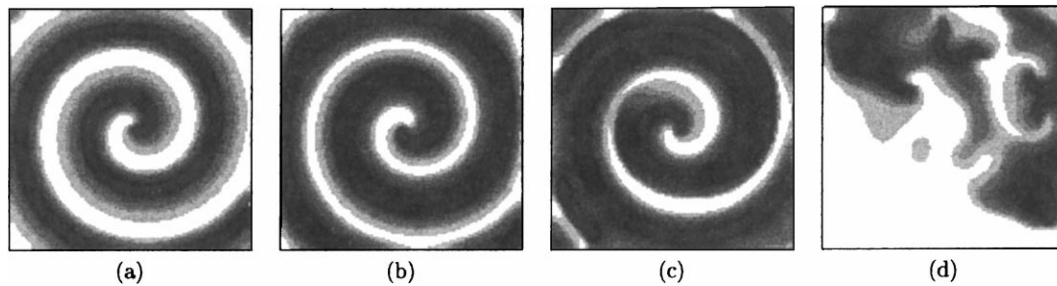


Fig. 4. Four snapshots of numerical integration for the first GLP, illustrating the loss of stability of a spiral when the value of  $P_C$  is changed (for  $P_O = 8$ ): (a)  $P_C = 3.375$ ; (b)  $P_C = 3.0$ . The spiral wavelength increases when the value of  $P_C$  decreases; (c)  $P_C = 2.5$ . However, the spiral becomes unstable and breaks into a regime of phase turbulence, as shown in (c) and (d), taken after time intervals of 30 units of time for the same value of  $P_C$ .

the second Hopf line to the right side of the diagram grants stability for the spirals at much larger values of  $P_{O_2}$  above the BF2 line. They are stable even in the small region above the BF1 and below the BF2 lines. Stability is lost for points close to the saddle-node line at the left side of the region and, for low values of  $P_{O_2}$  in the region surrounded by the Hopf line. These features are also present in the results for set 1.

A detailed analysis of the other different patterns which may emerge in the model requires the selection of appropriate initial conditions for the numerical integration. We have not carried such an analysis, but we have gathered indications of other possible patterns based on integrations where spirals failed to form or where they became unstable. For both GL parameter sets, we have observed the rare development of a mix of target and plane waves for some large values of  $P_{O_2}$ . But phase turbulence was the most common situation when spirals were destabilized, and seems to be the sole possible space dependent behavior in small  $P_{O_2}$  region. This is illustrated in Fig. 4. We have also noted the formation of a frozen aperiodic pattern close to the intersection of the Hopf and saddle-node line at the left side of the diagram. When  $P_{CO}$  is decreased, we note that the frozen structure starts to develop within the spiral core, and increases monotonically until it dominates the whole region. This process is different from the core instability reported elsewhere [33], which gives rise to intermittent behavior. As illustrated in Fig. 5, before the whole regions freezes, we note oscillations in the regions circumventing the small frozen spots.

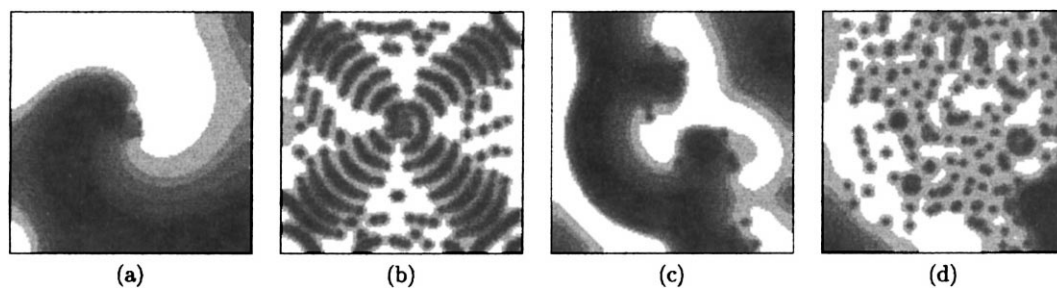


Fig. 5. Four snapshots illustrating the development of frozen aperiodic patterns after a spiral instability, for both GLPs. (a) and (b)  $P_C = 2.7$ ,  $P_O = 11$ , second set. A spiral generated by a single topological singularity at the center of the lattice breaks into a fairly regular concentric pattern, forming four fans and several irregularly placed spots. (c) and (d)  $P_C = 2.0$ ,  $P_O = 8$ , first set. The initial condition consists of random  $16 \times 16$  patches of cells with a constant value, which leads to several competing spirals, as those forming in (c). As they are unstable they give rise to a completely random frozen spot pattern shown in (d).

## 5. Conclusions

In this work, we have investigated the influence of different surface phase transitions on pattern selection in chemical reactions on single-crystal catalysts. We offered an explanation why the experiments performed with two quite similar simple reaction systems (CO oxidation on Pt(1 0 0) and on Pt(1 1 0)) have completely distinct behavior regarding the formation of spatio-temporal patterns. From the physical point of view, the major difference between the two systems is the first-order  $(1 \times 1) \leftrightarrow \text{hex}$  transition for Pt(1 0 0), in opposition to a second-order  $(1 \times 1) \leftrightarrow (1 \times 2)$  transition for Pt(1 1 0). The basic question that we addressed is whether a change in the nature of the transition may cause such a drastic change in the ability of the system in sustaining stable patterns.

We have used the ADB model, based on a set of four PDEs, which has been successful in describing the phase diagram for the oscillatory behavior of the Pt(1 0 0) oscillations. The dynamics of phase transition is described with the help of a GLP. Apart from the original values of GLP coefficients used to describe the original first-order transition, we selected a second set of coefficients, such that the barrier between the two phases is decreased, mimicking the situation of a hysteresis free second-order transition. We have concentrated on the stability of spiral waves, as this pattern has been experimentally observed on Pt(1 1 0) but not on Pt(1 0 0).

We proceeded a twofold analysis, based on the stability of solutions of the amplitude equations close to the Hopf transitions, as well as the numerical integration of the PDEs. We have found a fairly good agreement among the results obtained by the different methods. They indicate that spirals can be generated for both sets of GL parameters. However, we have shown that the region with stable spirals for the second set of coefficients is greatly enhanced. Results for an even higher barrier in the GL potential, not shown here, indicate that the region of stable spirals is still further reduced. Our results agree with the observed experimental facts, as they indicate that spiral patterns are easier to be observed in a model that describes the situation of a second-order phase transition. As we have kept constant all of the coefficients which are related to the chemical dynamics, we have strong evidences that the order of the transition really plays an important role in the stability of complex spatio-temporal patterns.

From a mathematical point of view, the enhancement of the region with stable spiral waves is motivated by the increase of the Hopf bifurcation lines at the border of the minimal oscillatory region.

Besides that, the present investigation has indicated new directions for future work on pattern formation of the model, as the presence of frozen spots discussed in Section 4.

## Acknowledgements

The authors are much indebted to Prof. G. Dewel for helpful discussions and critically reading the manuscript. DL and FBC thank the CNPq (Brazil) for financial support. RFSA is partially supported by the CNPq.

## Appendix A

Main steps for the evaluation of the coefficients  $\beta$  and  $\epsilon$  in (2.8) along the procedure by Kuramoto and Tsuzuki [32] are as follows:

1. Find the coordinates  $(\bar{w}, \bar{a})$  of FPs by equating to zero the r.h.s. of (2.6) and (2.7). Note that the Laplacian terms vanish, as we are seeking for stationary and homogeneous solutions. Numerical methods are required for evaluating the roots of the resulting polynomial equation of degree 7.
2. Make a coordinate transformation to new variables in the neighborhood of  $(\bar{w}, \bar{a})$ :

$$\tilde{w} = w - \bar{w}, \quad \tilde{a} = a - \bar{a}. \quad (\text{A.1})$$

3. From the linear part of the transformed equations obtain the  $2 \times 2$  matrix  $\mathbf{M}$  (of elements  $m_{ij}$ ):

$$\mathbf{M} = \begin{pmatrix} -k_2 + 2rk_7 P_{O_2}(1 - r\bar{w}/\bar{a}) & k_1 P_{CO}((1+q)/(1+\bar{a})^2) - k_7 P_{O_2}[1 + \alpha - (r\bar{w}/\bar{a})^2] \\ 1/\bar{a} & -\bar{w}/(\bar{a})^2 \end{pmatrix}. \quad (\text{A.2})$$

4. Write the coefficient  $\epsilon$  as

$$\epsilon = \frac{m_{11}(k_5 - k_9)}{\omega_0(k_5 + k_9)}, \quad (\text{A.3})$$

where  $\omega_0 = \sqrt{m_{11}m_{22} - m_{21}m_{12}}$  indicates the frequency of oscillation at the Hopf bifurcation.

5. Describe the nonlinear terms of second and third degree of the transformed equations with the help of constant  $2 \times 2$  matrices, multiplied to the right and to the left with the column vector

$$\begin{pmatrix} \tilde{w} \\ \tilde{a} \end{pmatrix}$$

and its transpose. Let  $\mathbf{P}_{(n)}$  and  $\mathbf{Q}_{(n)}$  ( $n = 2, 3$ ) indicate the matrices related to the equations for  $\tilde{w}$  and  $\tilde{a}$ , respectively. They read as

$$\mathbf{P}_{(2)} = \begin{pmatrix} -r^2k_7 P_{O_2}/\bar{a} & r^2k_7 P_{O_2}(\bar{w}/(\bar{a})^2) \\ r^2k_7 P_{O_2}(\bar{w}/(\bar{a})^2) & -qk_1 P_{CO}((1+q)/(1+\bar{a})^3) - r^2k_7 P_{O_2}((\bar{w})^2/(\bar{a})^3) \end{pmatrix}, \quad (\text{A.4})$$

$$\mathbf{P}_{(3)} = \begin{pmatrix} 0 & -2r^2k_7 P_{O_2}(\bar{w}/(\bar{a})^3) \\ r^2k_7 P_{O_2}/(\bar{a})^2 & q^2k_1 P_{CO}((1+q)/(1+\bar{a})^4) + r^2k_7 P_{O_2}((\bar{w})^2/(\bar{a})^4) \end{pmatrix}, \quad (\text{A.5})$$

$$\mathbf{Q}_{(2)} = \begin{pmatrix} 0 & -1/2(\bar{a})^2 \\ -1/2(\bar{a})^2 & -\bar{\eta}_3 - 3\bar{\eta}_4\bar{a} + \bar{w}/(\bar{a})^3 \end{pmatrix}, \quad (\text{A.6})$$

$$\mathbf{Q}_{(3)} = \begin{pmatrix} 0 & 1/(\bar{a})^3 \\ 0 & -\bar{\eta}_4 - \bar{w}/(\bar{a})^4 \end{pmatrix}. \quad (\text{A.7})$$

6. Define the coefficients:

$$J_0(0) = m_{11}m_{22} - m_{21}m_{12}, \quad J_0(2) = (m_{11} + 2i\omega_0)(m_{22} + 2i\omega_0) - m_{21}m_{12}. \quad (\text{A.8})$$

7. Define the matrices:

$$\mathbf{N}_{(2)} = (m_{22} + i\omega_0)\mathbf{P}_{(2)} - m_{12}\mathbf{Q}_{(2)}, \quad \mathbf{N}_{(3)} = (m_{22} + i\omega_0)\mathbf{P}_{(3)} - m_{12}\mathbf{Q}_{(3)}, \quad (\text{A.9})$$

$$\mathbf{L}_0(\mathbf{0}) = \begin{pmatrix} m_{22} & -m_{12} \\ -m_{21} & m_{11} \end{pmatrix}, \quad (\text{A.10})$$

$$\mathbf{L}_0(\mathbf{2}) = \begin{pmatrix} m_{22} + 2i\omega_0 & -m_{12} \\ -m_{21} & m_{11} + 2i\omega_0 \end{pmatrix}, \quad (\text{A.11})$$

$$\mathbf{C} = \begin{pmatrix} 1 & 0 \\ 0 & -(m_{11} + i\omega_0)/m_{12} \end{pmatrix}, \quad (\text{A.12})$$

and the column eigenvector at the Hopf bifurcation

$$\mathbf{c} = \begin{pmatrix} 1 \\ -(m_{11} + i\omega_0)/m_{12} \end{pmatrix}. \quad (\text{A.13})$$

8. Evaluate the coefficient:

$$g = 4J_0(0)^{-1} \mathbf{c}^t \mathbf{N}_2 \mathbf{L}_0(\mathbf{0}) \begin{pmatrix} \mathbf{c}^{*t} \mathbf{P}_2 \mathbf{c} \\ \mathbf{c}^{*t} \mathbf{Q}_2 \mathbf{c} \end{pmatrix} + 2J_0(2)^{-1} \mathbf{c}^{*t} \mathbf{N}_2 \mathbf{L}_0(\mathbf{2}) \begin{pmatrix} \mathbf{c}^t \mathbf{P}_2 \mathbf{c} \\ \mathbf{c}^t \mathbf{Q}_2 \mathbf{c} \end{pmatrix} + 2\mathbf{c}^t \mathbf{N}_3 \mathbf{C} \mathbf{c}^* + \mathbf{c}^{*t} \mathbf{N}_3 \mathbf{C} \mathbf{c}. \quad (\text{A.14})$$

9. Write the coefficient  $\beta$  as:

$$\beta = -\frac{\text{Re}(g)}{\text{Im}(g)}. \quad (\text{A.15})$$

## References

- [1] G. Ertl, Adv. Catal. 37 (1990) 213.
- [2] R. Imbihl, Prog. Surf. Sci. 44 (1993) 185.
- [3] R. Imbihl, G. Ertl, Chem. Rev. 95 (1995) 697.
- [4] L.F. Razon, R.A. Schmitz, Catal. Rev. Sci. Eng. 28 (1986) 89.
- [5] M.P. Cox, G. Ertl, R. Imbihl, Phys. Rev. Lett. 54 (1985) 1725.
- [6] R. Imbihl, M.P. Cox, G. Ertl, H. Müller, W. Brenning, J. Chem. Phys. 83 (1985) 1578.
- [7] R. Imbihl, M.P. Cox, G. Ertl, J. Chem. Phys. 84 (1986) 3519.
- [8] R.M. Eiswirth, G. Ertl, Surf. Sci. 177 (1986) 90.
- [9] A. Hopkinson, J.M. Bradley, X.-C. Guo, D.A. King, Phys. Rev. Lett. 71 (1993) 1597.
- [10] A. Hopkinson, D.A. King, Chem. Phys. 177 (1993) 433.
- [11] D.A. King, Surf. Rev. Lett. 1 (1994) 345.
- [12] M. Eiswirth, P. Möller, K. Wetzel, R. Imbihl, G. Ertl, J. Chem. Phys. 90 (1989) 510.
- [13] R.M. Eiswirth, K. Krischer, G. Ertl, Surf. Sci. 202 (1988) 565.
- [14] S. Jakubith, H.H. Rotermund, W. Engel, A. von Oertzen, G. Ertl, Phys. Rev. Lett. 65 (1990) 3013.
- [15] H.H. Rotermund, W. Engel, M. Kordesh, G. Ertl, Nature 343 (1990) 355.
- [16] A. von Oertzen, A.S. Mikhailov, H.H. Rotermund, G. Ertl, J. Phys. Chem. B 102 (1998) 4966.
- [17] K. Krischer, R.M. Eiswirth, G. Ertl, Surf. Sci. 251/252 (1991) 900.
- [18] K. Krischer, R.M. Eiswirth, G. Ertl, J. Chem. Phys. 96 (1992) 9161.
- [19] M. Bär, N. Gottschalk, R.M. Eiswirth, G. Ertl, J. Chem. Phys. 100 (1994) 1202.
- [20] P. Möller, K. Wetzel, M. Eiswirth, G. Ertl, J. Chem. Phys. 85 (1986) 5328.
- [21] R.F.S. Andrade, G. Dewel, P. Borckmans, J. Chem. Phys. 91 (1989) 2675.
- [22] R.F.S. Andrade, D. Lima, G. Dewel, P. Borckmans, J. Chem. Phys. 100 (1994) 9192.
- [23] D. Lima, R.F.S. Andrade, Braz. J. Phys. 24 (1994) 865.
- [24] L. Landau, E. Lifshitz, in: E. Lifshitz, L. Pitaevskii (Eds.), Statistical Physics, 3rd Edition, Part I, Pergamon Press, Oxford, 1984.
- [25] I.S. Aranson, L. Aranson, L. Kramer, A. Weber, Phys. Rev. A 46 (1992) 2992.
- [26] V.P. Zhdanov, K.I. Zamaraev, Sov. Phys. Usp. 29 (1986) 755.
- [27] V.P. Zhdanov, Surf. Sci. 426 (1999) 345.
- [28] M. Gruyters, T. Ali, D.A. King, Chem. Phys. Lett. 232 (1995) 1.
- [29] M. Gruyters, T. Ali, D.A. King, J. Phys. Chem. 100 (1996) 14417.
- [30] G.T. Rado, H. Suhl, Magnetism, Vol. 1, Academic Press, New York, 1963.
- [31] Y. Kuramoto, Chemical Oscillations, Waves and Turbulence, Springer, Berlin, 1984.
- [32] Y. Kuramoto, T. Tsuzuki, Prog. Theoret. Phys. 54 (1975) 687.
- [33] I. Aranson, L. Kramer, A. Weber, Phys. Rev. Lett. 72 (1994) 2316.